LUND UNIVERSITY

Time domain inversion techniques for electromagnetic scattering problems

Kristensson, Gerhard

1990

Link to publication

Citation for published version (APA):
Kristensson, G. (1990). *Time domain inversion techniques for electromagnetic scattering problems*. (Technical Report LUTEDX/(TEAT-7011)/1-33/(1990); Vol. TEAT-7011). [Publisher information missing].

Total number of authors:
1

General rights
Unless other specific re-use rights are stated the following general rights apply:
Copyright and moral rights for the publications made accessible in the public portal are retained by the authors and/or other copyright owners and it is a condition of accessing publications that users recognise and abide by the legal requirements associated with these rights.
- Users may download and print one copy of any publication from the public portal for the purpose of private study or research.
- You may not further distribute the material or use it for any profit-making activity or commercial gain
- You may freely distribute the URL identifying the publication in the public portal

Read more about Creative commons licenses: https://creativecommons.org/licenses/

Take down policy
If you believe that this document breaches copyright please contact us providing details, and we will remove access to the work immediately and investigate your claim.

LUND UNIVERSITY

PO Box 117
221 00 Lund
+46 46-222 00 00

CODEN:LUTEDX/(TEAT-7011)/1-33/(1990)

Time domain inversion techniques for electromagnetic scattering problems

Gerhard Kristensson

Department of Electroscience
Electromagnetic Theory
Lund Institute of Technology
Sweden

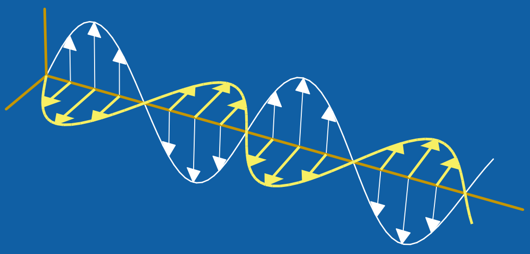

Gerhard Kristensson

Department of Electroscience
Electromagnetic Theory
Lund Institute of Technology
P.O. Box 118
SE-221 00 Lund
Sweden

Editor: Gerhard Kristensson
© Gerhard Kristensson, Lund, June 19, 2001

Abstract

This paper presents a review of and a comparison between two different methods to solve an inverse scattering problem in the time domain. The problem is that of propagation of transient electromagnetic waves in spatially inhomogeneous slabs of finite length. The permittivity and conductivity profiles are assumed to vary only with depth and the scattering problem is thus one-dimensional. Several algorithms to solve the direct and inverse scattering problems for continuous and discontinuous permittivity profiles are suggested. Some of these algorithms have not been published before. The aim of this paper is to compare and review these methods. More specifically, the numerical performance of the invariant imbedding approach (layer-stripping) and the Green functions formulation (downward continuation) is compared. Some new results based upon time reversal techniques for a lossless slab are presented in an appendix.

Notation

$c^{-2}(z) = \epsilon(z)\mu_0$

$b(z) = \sigma(z)\mu_0$

$x = x(z) = \int_0^z \frac{d\,z'}{lc(z')}$

$s = t/l$

$l = \int_0^L \frac{d\,z}{c(z)}$

$A(x) = -\frac{d}{d\,x} \ln c(z(x))$

$B(x) = -lb(z(x))c^2(z(x))$

$c_1 = \sqrt{\frac{\epsilon(L^+)}{\epsilon(L^-)}} = \frac{c(L^-)}{c(L^+)}$

$u^{\pm}(x,s) = \frac{1}{2}\left\{u(x,s) \mp \int_0^s u_x(x,s')d\,s'\right\}$

$\rho(x) = r\exp\left\{\int_x^1 B(x')d\,x'\right\}$

$r = (1-c_1)/(1+c_1)$

$\tau(x) = 2t^-(x,1)/(1+c_1)$

$t^{\pm}(x,y) = \exp\left\{\pm\int_x^y b^{\pm}(x')d\,x'\right\}$

$b^{\pm}(x) = \frac{1}{2}\left\{A(x) \pm B(x)\right\}$

$g(1) = \exp\left\{\int_0^1 B(x')\,dx'\right\}$

$a(1) = \frac{1}{2}b^-(1)g(1)$

1 Introduction

This paper is concerned with propagation of transient electromagnetic waves in lossy spatially inhomogeneous slabs of finite length. A homogeneous lossless medium is situated on either side of the slab and the permittivity and conductivity profiles are assumed to vary only with depth. The direct scattering problem is to calculate the scattering kernels from known permittivity and conductivity profiles. In the inverse problem these profiles are calculated from finite time traces of scattering data. These scattering problems have been analyzed both by scattering operator techniques (invariant imbedding), [3]– [6], and by Green functions techniques [7]. These two approaches are reviewed and compared in this paper. The two methods will be referred to as the invariant imbedding method or the layer-stripping method and the Green functions method or the downward continuation method, respectively. Special emphasis is made in comparing the numerical performance of the various algorithms in reconstructing the permittivity and conductivity profiles by using noisy data.

In Refs. [3]– [6], several algorithms based upon iteration schemes are suggested. In this paper, however, no attempts are made to cover these aspects of the inverse scattering problem. Therefore, only algorithms that utilize the basic equations in a non-iterative way are reviewed.

2 Basic equations

The geometry of the wave-scattering problem is such that the inhomogeneous slab occupies the region $0 \leq z \leq L$, see Figure 1. An electromagnetic plane wave is launched in the region $z < 0$ exterior to the slab. This field impinges normally on the medium, giving rise to an electric field $E(z,t)$ within the slab, with E satisfying

$$E_{zz}(z,t) - c^{-2}(z)E_{tt}(z,t) - b(z)E_t(z,t) = 0, \tag{2.1}$$

where

$$c^{-2}(z) = \epsilon(z)\mu_0, \qquad b(z) = \sigma(z)\mu_0,$$

and μ_0 is the permeability of vacuum. For simplicity, the permittivity profile is assumed to be continuously differentiable and the conductivity is assumed to be continuous in the interior of the slab. These assumptions can be relaxed. At the back edge, $z = L$, both the permittivity and the conductivity can have a finite jump discontinuity. In Ref. [5] it is shown that there is no loss of generality in assuming that the permittivity profile is continuous at the front edge, $z = 0$. More explicitly, the scattering problem with finite jump discontinuities in the permittivity profile at the front and back edges, $z = 0$ and $z = L$, respectively, can always be reduced to a problem with only a finite jump discontinuity at the back edge, $z = L$. In this paper it is therefore assumed that the permittivity is continuous at the front edge. This removal of jump discontinuities at the edges of the slab can also be carried out at the back edge, $z = L$. It is, however, advantageous for the solution of the inverse scattering problem to retain the back edge jump discontinuity, if there is one present.

In order to facilitate the numerical computations a conversion to travel time coordinates is made. These coordinates are defined as

$$\begin{aligned} x &= x(z) = \int_0^z \frac{d\,z'}{lc(z')}, \\ s &= t/l, \\ \\ u(x,s) &= E(z,t), \end{aligned}$$

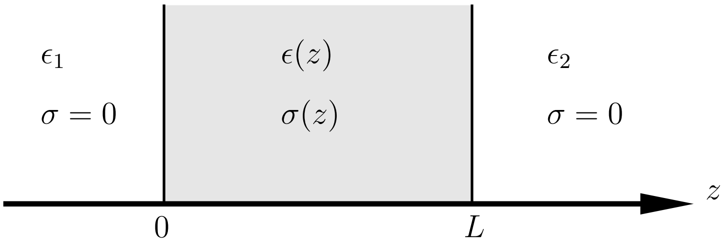

Figure 1: The geometry of the slab.

where

$$l = \int_0^L \frac{dz}{c(z)}.$$

This transformation maps the slab into the region $[0, 1]$. The time coordinate s is normalized so that $s = 1$ is the time it takes for the wave front to travel through the slab once. A round trip through the slab will then be $s = 2$. The wave equation (2.1) then transforms into

$$u_{xx}(x, s) - u_{ss}(x, s) + A(x)u_x(x, s) + B(x)u_s(x, s) = 0, \tag{2.2}$$

where

$$A(x) = -\frac{d}{dx} \ln c(z(x)),$$

$$B(x) = -lb(z(x))c^2(z(x)).$$

From the knowledge of the two functions $A(x)$ and $B(x)$, the constant l, and the value of $\epsilon(0)$, it is possible to reconstruct the depth z, the permittivity $\epsilon(z)$, and the conductivity $\sigma(z)$.

$$\left\{\begin{array}{ll} z(x) = \dfrac{l}{\sqrt{\mu_0 \epsilon(0)}} \displaystyle\int_0^x \exp\left\{ -\int_0^{x'} A(x'')\,dx'' \right\} dx', & \\ \epsilon(z(x)) = \epsilon(0) \exp\left\{ 2 \displaystyle\int_0^x A(x')\,dx' \right\}, & 0 < x < 1, \\ \sigma(z(x)) = -\dfrac{\epsilon(0)B(x)}{l} \exp\left\{ 2 \displaystyle\int_0^x A(x')\,dx' \right\}. & \end{array}\right. \tag{2.3}$$

The boundary conditions at the edges are the continuity in the transverse electric and magnetic fields. With the assumptions made on the permittivity profile above, these boundary conditions are

$$u(0^+, s) = u(0^-, s),$$
$$u_x(0^+, s) = u_x(0^-, s),$$

at the front edge. The discontinuity in the permittivity profile at the back edge of the slab, $x = 1$, however, gives a discontinuity in the spatial derivative of $u(x, s)$. The boundary conditions at the back edge are therefore

$$\begin{aligned} u(1^+, s) &= u(1^-, s), \\ c_1 u_x(1^+, s) &= u_x(1^-, s), \end{aligned}$$

where

$$c_1 = \sqrt{\frac{\epsilon(L^+)}{\epsilon(L^-)}} = \frac{c(L^-)}{c(L^+)}.$$

This constant c_1 is a measure of the jump discontinuity at the back edge. The completely continuous profile then corresponds to $c_1 = 1$, and the problem of a slab with a perfectly conducting wall at $x = 1$ corresponds to $c_1 \to \infty$.

The keystone in the two formulations that are treated in this paper is the wave splitting concept. The wave splitting is defined as [1]

$$u^{\pm}(x, s) = \frac{1}{2}\left\{ u(x, s) \mp \int_0^s u_x(x, s')d\,s' \right\}. \tag{2.4}$$

This transformation is symbolically depicted in Figure 2. In a homogeneous lossless region the wave splitting, (2.4), projects out the left- and right-going parts, respectively, of the solution. In a non-homogeneous region, (2.4) generalizes this projection always having

$$u(x, s) = u^+(x, s) + u^-(x, s),$$

everywhere.

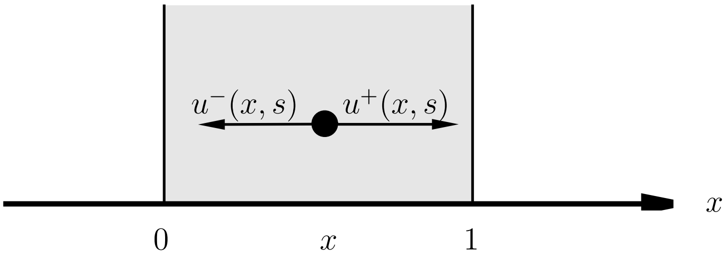

Figure 2: The wave splitting.

3 Invariant imbedding formulation

This section presents the scattering operator formulation of the scattering problem in an invariant imbedding setting.

Consider a subsection $[x, 1]$ of the physical region $[0, 1]$, see Figure 3. Mathematically, the original problem, $[0, 1]$, is imbedded in a family of problems where the left edge of the slab, x, is the parameter that is varied.

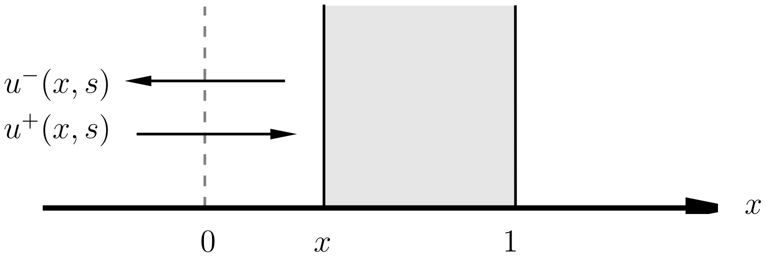

Figure 3: The geometry of the subsection problem $[x,1]$.

3.1 Basic equations

The fields $u^+(x,s)$ and $u^-(x,s)$, defined at the position x, are related to each other by the scattering operators. This relation is represented as an integral operator, where the scattering kernels $R^+(x,s)$ and $T(x,s)$ are defined for $s>0$ by [5]

$$\begin{cases} u^-(x,s)=\rho(x)u^+(x,s-2(1-x))+\displaystyle\int_0^s R^+(x,s-s')u^+(x,s')d\,s', \\ u^+(1,s+1-x)=\tau(x)\left\{u^+(x,s)+\displaystyle\int_0^s T(x,s-s')u^+(x,s')d\,s'\right\}, \end{cases} \tag{3.1}$$

where

$$\begin{cases} \rho(x)=r\exp\left\{\displaystyle\int_x^1 B(x')d\,x'\right\}=\rho(0)\exp\left\{-\displaystyle\int_0^x B(x')d\,x'\right\}, \\ \tau(x)=2t^-(x,1)/(1+c_1), \\ r=(1-c_1)/(1+c_1), \end{cases}$$

and[1]

$$\begin{cases} t^\pm(x,y)=\exp\left\{\pm\displaystyle\int_x^y b^\pm(x')d\,x'\right\}, \\ b^\pm(x)=\dfrac{1}{2}\left\{A(x)\pm B(x)\right\}. \end{cases}$$

The kernels $R^+(x,s)$ and $T(x,s)$ can be interpreted as the reflection and the transmission kernels, respectively, for the subsection $[x,1]$, where the medium to the left of x is of constant permittivity $\epsilon(z(x))$. The field $u^+(x,s)$ serves as an incident field, while $u^-(x,s)$ is a reflected field, for this subsection problem. For the special value $x=0$, the physical reflection and transmission kernels for the scattering problem are denoted $R^+(s)=R^+(0,s)$ and $T(s)=T(0,s)$, respectively.

---

[1] Note the sign change in the definition of $t^\pm(x,y)$ compared to [3]– [6].

Hence, the reflection and transmission kernels, $R^+(s)$ and $T(s)$, for the physical region $[0,1]$ is imbedded in a family of subsection problems $[x,1]$ with reflection and transmission kernels $R^+(x,s)$ and $T(x,s)$, respectively.

The reflection kernel $R^+(x,s)$ satisfies a non-linear integro-differential equation that is related to the Riccati equation. Lengthy but straightforward calculations give the imbedding equation for the reflection kernel $R^+(x,s)$ [5]

$$\begin{aligned} R^+_x(x,s) &= 2R^+_s(x,s) - B(x)R^+(x,s) - b^+(x)\int_0^s R^+(x,s-s')R^+(x,s')\,ds' \\ &\quad -2H(s-2(1-x))\rho(x)b^+(x)R^+(x,s-2(1-x)), \quad s>0, \qquad (3.2)\\ R^+(1,s) &= 0, \quad s>0, \\ R^+(x,0^+) &= -\frac{1}{2}b^-(x), \quad 0<x<1, \qquad (3.3) \end{aligned}$$

where $H(s)$ is the Heaviside function $H(s) = \begin{cases} 0, & s<0, \\ 1, & s>0. \end{cases}$

The reflection kernel $R^+(x,s)$ is a continuous function except along the lines $s = 2(1-x)$ and $s = 4(1-x)$ where the kernel has finite jump discontinuities. These jumps are

$$\begin{aligned} \left[R^+(x,s)\right]_{s=2(1-x)^-}^{s=2(1-x)^+} &= \frac{1}{2}\exp\left\{\int_x^1 B(x')\,dx'\right\} \\ &\quad \times\left\{r^2b^+(1) + b^-(1) - 2r\int_x^1 b^+(x')b^-(x')\,dx'\right\}, \qquad (3.4)\\ \left[R^+(x,s)\right]_{s=4(1-x)^-}^{s=4(1-x)^+} &= -\frac{1}{2}\rho^2(x)b^+(x). \end{aligned}$$

Similar to the derivation of the imbedding equation of the reflection kernel above, it can be proved that the transmission kernel also satisfies an imbedding equation. The imbedding equation for the transmission kernel $T(x,s)$ is

$$\begin{aligned} T_x(x,s) &= -b^+(x)\Big\{R^+(x,s) + \int_0^s T(x,s-s')R^+(x,s')\,ds' \\ &\quad + H(s-2(1-x))\rho(x)T(x,s-2(1-x))\Big\}, \quad s>0, \qquad (3.5)\\ T(1,s) &= 0, \quad s>0. \end{aligned}$$

The transmission kernel is a continuous function except along the line $s = 2(1-x)$ where the kernel has a finite jump discontinuity

$$[T(x,s)]_{s=2(1-x)^-}^{s=2(1-x)^+} = -\frac{1}{2}\rho(x)b^+(x).$$

Of fundamental importance for the analysis presented in this paper is the resolvent of the transmission kernel. The resolvent equation defines the propagator kernel $W(x,s)$.

$$T(x,s) + W(x,s) + \int_0^s T(x,s-s')W(x,s')\,ds', \quad s>0. \qquad (3.6)$$

The imbedding equation for the propagator kernel $W(x,s)$ is similar to the one for the transmission kernel.

$$\begin{aligned} W_x(x,s) = b^+(x)\Big\{ & R^+(x,s) + \int_0^s W(x,s-s')R^+(x,s')d\,s' \\ & +H(s-2(1-x))\rho(x)W(x,s-2(1-x))\Big\}, \quad s>0. \end{aligned} \tag{3.7}$$

The propagator kernel $W(x,s)$ has a fundamental property that the other kernels $R^+(x,s)$ and $T(x,s)$ do not have. The propagator kernel $W(x,s)$ has compact support in $[0,2(1-x)]$ and the value at $s=2(1-x)^-$ is

$$W(x,2(1-x)^-) = -\frac{1}{2}\rho(x)b^+(x). \tag{3.8}$$

This fact is used below in the solution of the inverse scattering problem.

3.2 Special case, $c_1 = 1$

The special case of no back wall, $c_1 = 1$, leads to simplifications. In this special case, reflection from the right hand side is employed in the solution of the inverse problem. The scattering kernel $R^-(x,s)$ is defined in analogy with the kernels $R^+(x,s)$ and $T(x,s)$ above, i.e., $R^-(x,s)$ is the reflection kernel for the subsection problem $[x,1]$ for an excitation impinging from the right, $z>L$. The physical kernel is denoted $R^-(s) = R^-(0,s)$ in analogy with the notations $R^+(s)$ and $T(s)$. The following properties of the reflection kernel $R^-(x,s)$ are important for the solution of the inverse problem [3]:

$$\big[R^-(x,s)\big]_{s=2(1-x)^-}^{s=2(1-x)^+} = -\frac{1}{2}b^+(x)\exp\left\{\int_x^1 B(x')\,dx'\right\}, \tag{3.9}$$

$$R^-(x,s) = R^-(0,s) = R^-(s), \quad s<2(1-x). \tag{3.10}$$

4 The Green function formulation

The scattering operator representations between the fields $u^+(x,s)$ and $u^-(x,s)$ in Section 3 are defined at the position x. It is also possible to relate the fields $u^+(x,s)$ and $u^-(x,s)$ to the external excitation $u^+(0,s)$, see Figure 4.

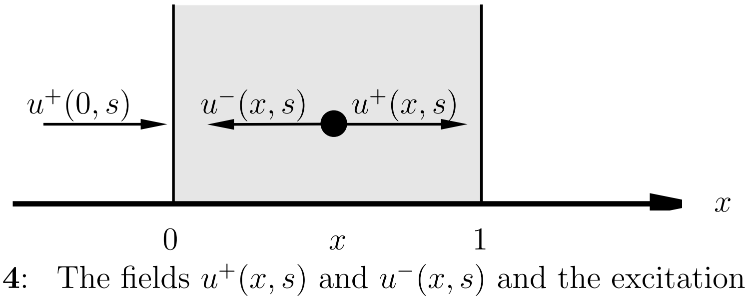

Figure 4: The fields $u^+(x,s)$ and $u^-(x,s)$ and the excitation $u^+(0,s)$.

4.1 Basic equations

The definition of the Green functions for $s > 0$ are [7]

$$\begin{cases} u^+(x,s) = t^-(0,x)\Big\{u^+(0,s-x) \\ \qquad\qquad + \displaystyle\int_0^{s-x} G_1(x,s-s')u^+(0,s')d\,s'\Big\}, \\ u^-(x,s) = \left[t^+(0,x)\right]^{-1}\Big\{\rho(0)u^+(0,s+x-2) \\ \qquad\qquad + \displaystyle\int_0^{s-x} G_2(x,s-s')u^+(0,s')d\,s'\Big\}. \end{cases} \tag{4.1}$$

These relations are derived in analogy with the ones in equation (3.1).

The Green functions satisfy a set of coupled partial differential equations, which are derived in a similar manner as (3.2) [7]

$$\begin{cases} \partial_x G_1(x,s) + \partial_s G_1(x,s) = b^+(x)\exp\left\{-\int_0^x B(x')d\,x'\right\}G_2(x,s), \\ \partial_x G_2(x,s) - \partial_s G_2(x,s) = b^-(x)\exp\left\{\int_0^x B(x')d\,x'\right\}G_1(x,s), \end{cases} \tag{4.2}$$

$$\begin{aligned} &G_1(0,s) = 0, \\ &G_2(1,s) = \rho(0)G_1(1,s), \\ &G_1(x,x^+) = -\frac{1}{2}\int_0^x b^+(x')b^-(x')d\,x', \\ &G_2(x,x^+) = -\frac{1}{2}b^-(x)\exp\left\{\int_0^x B(x')d\,x'\right\}. \end{aligned} \tag{4.3}$$

The Green functions $G_1(x,s)$ and $G_2(x,s)$ are continuous everywhere except along the lines $s = 2\pm x$, where $G_1(x,s)$ and $G_2(x,s)$ have finite jump discontinuities.

$$[G_1(x,s)]_{s=(2-x)^-}^{s=(2-x)^+} = \frac{1}{2}b^+(x)\rho(x), \tag{4.4}$$

$$\begin{aligned} [G_1(x,s)]_{s=(2+x)^-}^{s=(2+x)^+} &= -\frac{1}{2}b^+(0)\rho(0), \\ [G_2(x,s)]_{s=(2-x)^-}^{s=(2-x)^+} &= \frac{1}{2}b^-(1)\exp\left\{\int_0^1 B(x')d\,x'\right\} \\ &+\frac{1}{2}\rho(0)\left\{-\int_0^1 b^+(x)b^-(x)d\,x - \int_x^1 b^+(x')b^-(x')d\,x'\right\} + \frac{1}{2}r\rho(0)b^+(1). \end{aligned} \tag{4.5}$$

In addition to the jumps above, the Green function $G_2(x,s)$ has a finite jump discontinuity at $s = 4-x$.

$$[G_2(x,s)]_{s=(4-x)^-}^{s=(4-x)^+} = -\frac{1}{2}\rho(0)^2 b^+(0).$$

The Green functions are, of course, related to the physical scattering operators that were analyzed in Section 3. These relations between the Green functions and the scattering operators are given as relations at the boundaries of the slab, i.e., at $x = 0$ and $x = 1$ as easily seen from (3.1) and (4.1). The result is

$$\begin{cases} G_2(0, s) = R^+(s), \\ G_1(1, s+1) = T(s). \end{cases}$$

5 Extension of data

A very useful property, which also is the one that solves the inverse scattering problems in Sections 7.1.1, 7.2.2, 8.1.2 and 8.2, is the concept of extension of data. In Ref. [3] it is proved that one round trip of transmission data, i.e., $T(s)$, $0 < s < 2$, suffices to uniquely calculate transmission data for later times, i.e., $s > 2$. This extension concept relies on the special property that the propagator kernel W has compact support in the time interval of one round trip. The extension of data can be formulated for the subsection problem $[x, 1]$, and the following equation holds:

$$T(x, s) + \int_{2(1-x)}^{s} W(x, s-s')T(x, s')d\,s' = G(x, s), \quad s > 2(1-x), \tag{5.1}$$

where

$$G(x, s) = \begin{cases} -\displaystyle\int_{s-2(1-x)}^{2(1-x)} W(x, s-s')T(x, s')d\,s', & 2(1-x) < s < 4(1-x), \\ 0, & s > 4(1-x). \end{cases}$$

If transmission data $T(x, s)$ are known for one round trip, i.e., $0 < s < 2(1-x)$, then the function $G(x, s)$ is known, since the propagator kernel $W(x, s)$ is known everywhere. Equation (5.1), which is a Volterra equation of the second kind, can then be solved uniquely for the unknown transmission kernel $T(x, s)$, $s > 2(1-x)$.

A similar extension property holds for the reflection data $R^{\pm}$. However, this time transmission data as well as reflection data have to be known for one round trip in order to calculate the reflection data for times greater than one round trip. Transmission data are needed to get the propagator kernel W. The basic equation for extension of reflection data is [3]

$$\begin{aligned} R^{\pm}(x, s) + \int_{2(1-x)}^{s} W(x, s-s')R^{\pm}(x, s')d\,s' = \\ g(x, s) - \rho(x)W(x, s-2(1-x)), \quad s > 2(1-x), \end{aligned} \tag{5.2}$$

where

$$g(x, s) = \begin{cases} -\displaystyle\int_{s-2(1-x)}^{2(1-x)} W(x, s-s')R^{\pm}(x, s')d\,s', & 2(1-x) < s < 4(1-x), \\ 0, & s > 4(1-x). \end{cases}$$

This is again a Volterra equation of the second kind for the unknown $R^{\pm}(x,s)$, $s > 2(1-x)$.

Moreover, the Green functions, G_1 and G_2, satisfy a similar extension property as the ones given for $R^{\pm}(x,s)$ and $T(x,s)$ above. In particular, for G_1 and G_2 it can be demonstrated that [7]

$$G_1(x,s) + \int_{2-x}^{s} G_1(x,s')W(0,s-s')\,ds' = F(x,s), \quad s > 2-x, \tag{5.3}$$

$$G_2(x,s) + \int_{2-x}^{s} G_2(x,s')W(0,s-s')\,ds' = f(x,s), \quad s > 2-x, \tag{5.4}$$

where

$$F(x,s) = \begin{cases} -W(0,s-x) - \displaystyle\int_{x}^{2-x} G_1(x,s')W(0,s-s')\,ds', & 2-x < s < 2+x, \\ -\displaystyle\int_{s-2}^{2-x} G_1(x,s')W(0,s-s')\,ds', & 2+x < s < 4-x, \\ 0, & s > 4-x, \end{cases}$$

and

$$f(x,s) = \begin{cases} -\displaystyle\int_{\max(x,s-2)}^{2-x} G_2(x,s')W(0,s-s')\,ds' \\ \qquad\qquad - \rho(0)W(0,s+x-2), & 2-x < s < 4-x, \\ 0, & s > 4-x. \end{cases}$$

and where the propagator kernel $W(0,s)$ is the resolvent kernel of the physical transmission kernel, $T(0,s) = T(s)$. Notice that these equations are Volterra second kind equations for $G_1(x,s)$ and $G_2(x,s)$ above the line $s = 2-x$, so once G_1 is known below that line, it is known above the line and similarly for G_2.

6 Layer-stripping vs. downward continuation in the lossless case

In this section inversion algorithms for the simpler case of a lossless profile, $\sigma = 0$, are considered. This case is included in this paper merely for completeness. Some new results, however, on the properties of the reflection and the transmission kernels are found in Appendix A. These results are proved by employing the concept of time reversion. Several new integral relations and inequalities for the reflection and the transmission kernels are proved.

The inverse problem here is to find the permittivity profile $\epsilon(z)$ from a finite time trace of reflection data. This inverse problem has been presented in [1] for the scattering operator approach or layer-stripping method, but for completeness and comparison this method is reviewed here together with the approach based upon the Green function approach. Numerical illustrations can be found in [1].

Sufficient data set for a reconstruction of the permittivity profile $\epsilon(z)$ is given in Table 1 [1]. These data suffice for both the downward continuation and the layer-stripping method. The two constants l and $\epsilon(0)$ are needed to transform the function $A(x)$ back to the physical quantities $z(x)$ and $\epsilon(z)$, see (2.3).

Data set for inversion
$R^+(s), \quad 0 < s < 2$
l
$\epsilon(0)$

Table 1: The data set for inversion of the lossless permittivity profile.

6.1 Layer-stripping

The inverse problem using the imbedding equations is solved by the following equations, which are special cases of (3.2) and (3.3):

$$\begin{aligned} R^+_x(x,s) &= \\ &2R^+_s(x,s) - \frac{1}{2}A(x)\int_0^s R^+(x,s-s')R^+(x,s')d\,x', \quad 0 < s < 2(1-x), \quad (6.1) \\ R^+(x,0^+) &= -\frac{1}{4}A(x), \quad (6.2) \end{aligned}$$

and where $0 < x < 1$.

The inversion algorithm using the invariant imbedding equations then proceeds as follows:

1) Use (6.1) to implicitly step a portion of R^+ forward in the x-direction to the grid point $(x_1, 0)$, where $x_1 = x_0 + h$.
2) Compute $A(x_1)$ from (6.2).
3) Use (6.1) to implicitly step the remaining $R^+(x_0, s)$ data forward in the x-direction to the set of grid points at x_1 for $0 < s < 2(1-x_1)$.
4) Repeat steps 1-3 to move one grid line deeper into the medium.

6.2 Downward continuation

The inverse problem using the Green functions equations is solved by the following equations, which are special cases of (4.2) and (4.3):

$$\begin{cases} \partial_x G_1(x,s) + \partial_s G_1(x,s) = \frac{1}{2} A(x) G_2(x,s), \\ \partial_x G_2(x,s) - \partial_s G_2(x,s) = \frac{1}{2} A(x) G_1(x,s), \end{cases} \quad x < s < 2-x, \tag{6.3}$$

$$G_2(x,x^+) = -\frac{1}{4} A(x), \tag{6.4}$$

and where $0 < x < 1$.

The inversion algorithm using the Green functions technique then proceeds as follows:

1) Use (6.3) to implicitly step G_2 forward in the x-direction to the grid point (x_1, x_1), where $x_1 = x_0 + h$.

2) Compute $A(x_1)$ from (6.4).

3) Use (6.3) to implicitly step the remaining $G_1(x_0, s)$ and $G_2(x_0, s)$ data forward in the x-direction to the set of grid points at x_1 for $x_1 < s < 2 - x_1$.

4) Repeat steps 1-3 to move one grid line deeper into the medium.

This algorithm is, in general, one order of magnitude faster than the algorithm based upon the invariant imbedding equation in Section 6.1, due to the absence of convolution integrals.

7 Layer-stripping vs. downward continuation in a lossy case with no back wall

This is the case of a completely continuous permittivity profile. With the notation defined in Section 2, this corresponds to $c_1 = 1$. Some special considerations have already been given in Section 3.2. At present, it seems only the invariant imbedding equations generate a robust method. This algorithm is presented in Section 7.1. Two additional algorithms based upon the imbedding equations and the Green functions, respectively, are presented in Section 7.2. These two inversion algorithms utilize a smaller data set, and they are considerably less stable.

7.1 T, R^+ and R^- data given

The details of the inversion algorithm using the invariant imbedding equations given in this section can be found in Refs. [3, 4]. No algorithm based upon the Green functions technique is at present available that uses this data set.

The data set for inversion is given in Table 2 [4]. This data set implies that measurements have to be performed with sources on both sides of the slab. This data set is the largest data set used in this paper. As in the lossless case the two constants l and $\epsilon(0)$ are needed to transform the two functions $A(x)$ and $B(x)$ back to the physical quantities $z(x)$, $\epsilon(z)$ and $\sigma(z)$, see (2.3). The constant $g(1) = t^+(0,1)t^-(0,1)$ is assumed to be extracted from the knowledge of $t^+(0,1)$ and $t^-(0,1)$ through the transmission experiments [4].

Data set for inversion
$R^+(s), \quad 0 < s < 2$
$R^-(s), \quad 0 < s < 2$
$T(s), \quad 0 < s < 2$
$g(1) = \exp\left\{\int_0^1 B(x')\,dx'\right\}$
l
$\epsilon(0)$

Table 2: The first data set for inversion of the continuous lossy permittivity profile.

7.1.1 Layer-stripping

The jump in $R^-(x,s)$ at $s = 2(1-x)$, given by (3.9), can be rewritten using the extension of data in (5.2). If equation (3.10) is also used the result is

$$\begin{aligned}\int_0^{2(1-x)} & W(x,2(1-x)-s')R^-(0,s')d\,s' + R^-(0,2(1-x)^-) \\ &= \frac{1}{2}b^+(x)\exp\left\{\int_x^1 B(x')\,dx'\right\}. \qquad (7.1)\end{aligned}$$

The inverse problem, i.e., to recover $A(x)$ and $B(x)$, using the invariant imbedding equations is solved by employing the following equations as suggested in [4]:

$$\begin{aligned}
&R_x^+(x,s) = 2R_s^+(x,s) - B(x)R^+(x,s) \\
&\quad -b^+(x)\int_0^s R^+(x,s-s')R^+(x,s')d\,x', \quad 0 < s < 2(1-x), && (7.2)\\
&W_x(x,s) = \\
&\quad b^+(x)\left\{R^+(x,s) + \int_0^s W(x,s-s')R^+(x,s')d\,s'\right\}, \quad 0 < s < 2(1-x), && (7.3)\\
&R^+(x,0^+) = -\frac{1}{2}b^-(x), && (7.4)\\
&\int_0^{2(1-x)} W(x,2(1-x)-s')R^-(0,s')d\,s' + R^-(0,2(1-x)^-) \\
&\quad = \frac{1}{2}b^+(x)g(1)\exp\left\{-\int_0^x B(x')\,dx'\right\}, && (7.5)
\end{aligned}$$

and where $0 < x < 1$. These four equations are special cases of equations (3.2), (3.7), (3.3) and (7.1).

The inversion algorithm using the invariant imbedding equations then proceeds as follows:

1) Use (7.3) to explicitly step W from the current grid line x_0 to the next grid line $x_1 = x_0 + h$ for $0 < s < 2(1 - x_1)$.

2) Use (7.2) to implicitly step a portion of R^+ forward in the x-direction to the grid point $(x_1, 0)$.

3) To estimate $A(x_1)$ and $B(x_1)$, set $x = x_1$ in (7.4) and (7.5). In this case, one of these coefficients is found by solving a quadratic equation, and the other is found by simple substitution.

4) Use (7.2) to implicitly step the remaining $R^+(x_0, s)$ data forward in the x-direction to the set of grid points at x_1 for $0 < s < 2(1 - x_1)$.

5) Repeat steps 1-4 to move one grid line deeper into the medium.

The accuracy of this algorithm can be considerably improved through the use of iteration. All that needs to be done is to add the following steps after step 4:

4a) Use (7.3) to implicitly step W from the current grid line x_0 to the next grid line x_1 for $0 < s < 2(1 - x_1)$. This can be done since A, B and R^+ are known (to some degree of accuracy) on the grid lines x_0 and x_1.

4b) Go to step 2.

7.1.2 Numerical experiments

Figures 5 and 6 illustrate the inversion of noise-free data using the layer-stripping algorithm. More numerical examples are found in [4]. As seen from Figures 5 and 6 excellent agreement with the true profile is obtained in the reconstructions using the data set in Table 2.

Figures 7 and 8 illustrate how the algorithm reconstructs the permittivity and the conductivity profiles with noisy data. Gaussian noise with STD=0.05 has been added to the reflection data, R^+, R^-, and the transmission data T. This correspond to a S/N ratio of 5.4 for the reflection kernels, and 2.2 for the transmission kernel. The reconstruction of the conductivity found in Figure 8 clearly demonstrates that the reconstruction of the deeper portions of the medium is quite good in spite of fairly noisy data. The reconstruction of the permittivity is always one order smoother than the reconstruction of the conductivity, see (2.3). This algorithm, based upon the imbedding equations, satisfies the criteria of stability very well.

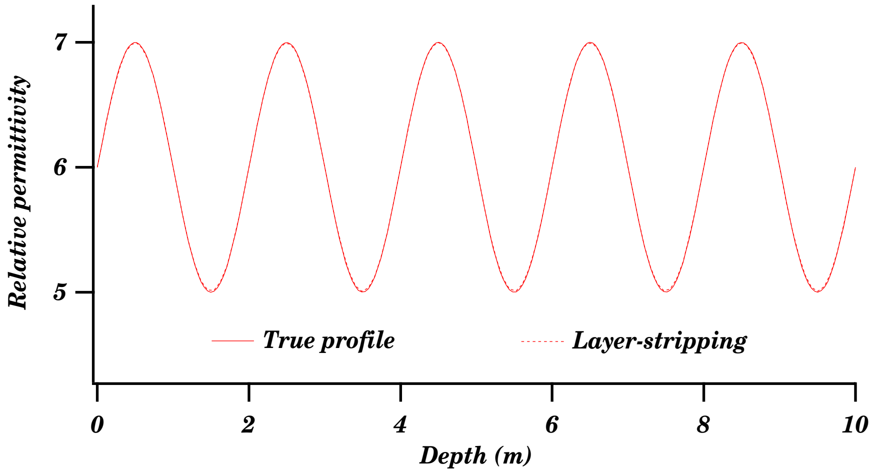

Figure 5: The reconstruction of the relative permittivity profile without a back wall using noise-free R^+, T and R^- data. Three iterations to improve the reconstruction in $A(x)$ and $B(x)$ are made.

7.2 T and R^+ data given

This data set uses only measurements from an experiment with sources on one side of the slab. However, the algorithms presented below are considerably less robust compared with the one given in Section 7.1 that uses data from a two-sided experiment. The lack of robustness is due to differentiation of data. This sensitivity clearly shows up in the numerical illustrations in Section 7.2.3.

The data set for inversion is given in Table 3. This data set is smaller than the one given in Table 2.

Data set for inversion
$R^+(s), \quad 0 < s < 2$
$T(s), \quad 0 < s < 2$
l
$\epsilon(0)$

Table 3: The second data set for inversion of the continuous lossy permittivity profile.

7.2.1 Layer-stripping

In the layer-stripping algorithm presented in Section 7.1.1 the jump discontinuity in the reflection kernel R^- was used in recovering the functions $A(x)$ and $B(x)$. In this algorithm, the jump discontinuity in the reflection kernel $R^+(x,s)$ at $s = 2(1-x)$ is utilized.

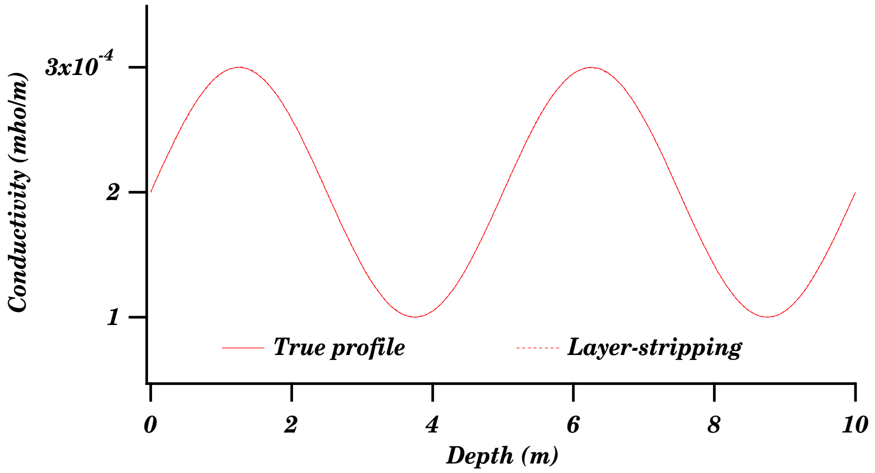

Figure 6: The reconstruction of the conductivity profile without a back wall using noise-free R^+, T and R^- data. Three iterations to improve the reconstruction in $A(x)$ and $B(x)$ are made.

The propagator kernel $W(x,s)$ is continuous at $s = 2(1-x)$ and $W(x, 2(1-x)^+) = W(x, 2(1-x)^-) = 0$, see (3.8). This yields

$$[W_x(x,s)]_{s=2(1-x)^-}^{s=2(1-x)^+} = 2\,[W_s(x,s)]_{s=2(1-x)^-}^{s=2(1-x)^+} = -2W_s(x, 2(1-x)^-).$$

The jump condition of $R^+(x,s)$ at $s = 2(1-x)$, see (3.4), and the imbedding equation for $W(x,s)$, see (3.7), therefore, imply that

$$\begin{aligned} -2W_s(x, 2(1-x)^-) &= b^+(x)\left[R^+(x,s)\right]_{s=2(1-x)^-}^{s=2(1-x)^+} \\ &= b^+(x)a(1)\exp\left\{-\int_0^x B(x')\,dx'\right\}, \end{aligned} \qquad (7.6)$$

where $a(1) = \frac{1}{2}b^-(1)\exp\left\{\int_0^1 B(x')\,dx'\right\}$.

The inverse problem using the invariant imbedding equations is solved by the following equations:

$$\begin{aligned} R_x^+(x,s) &= 2R_s^+(x,s) - B(x)R^+(x,s) \\ &\quad -b^+(x)\int_0^s R^+(x,s-s')R^+(x,s')d\,x', \quad 0 < s < 2(1-x), \end{aligned} \qquad (7.7)$$

$$\begin{aligned} &W_x(x,s) = \\ &\quad b^+(x)\left\{R^+(x,s) + \int_0^s W(x,s-s')R^+(x,s')d\,s'\right\}, \quad 0 < s < 2(1-x), \end{aligned} \qquad (7.8)$$

$$R^+(x,0^+) = -\frac{1}{2}b^-(x), \qquad (7.9)$$

$$W_s(x, 2(1-x)^-) = -\frac{1}{2}b^+(x)a(1)\exp\left\{-\int_0^x B(x')\,dx'\right\}, \qquad (7.10)$$

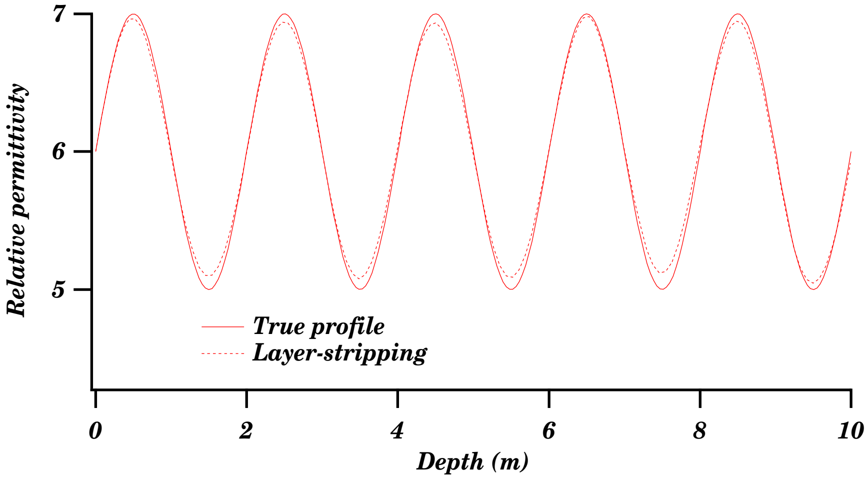

Figure 7: The reconstruction of the relative permittivity profile without a back wall using noisy data. Gaussian noise with STD=0.05 has been added to the reflection data, R^+, R^-, and the transmission data T. The data are smoothed once before inversion. Three iterations to improve the reconstruction in $A(x)$ and $B(x)$ are made.

and where $0 < x < 1$. These four equations are special cases of equations (3.2), (3.7), (3.3) and (7.6). The value of the propagator kernel at one round trip, $W_s(x, 2(1-x)^-)$, is computed by numerical differentiation. The constant $a(1)$ can be obtained by extension of data since the jump discontinuity for the physical reflection kernel $R^+(s)$ is, see (3.4) evaluated at $x = 0$

$$\left[R^+(s)\right]_{s=2^-}^{s=2^+} = a(1).$$

The inversion algorithm using the invariant imbedding equations then proceeds as follows:

1) Use (7.8) to explicitly step W from the current grid line x_0 to the next grid line $x_1 = x_0 + h$ for $0 < s < 2(1 - x_1)$.

2) Use (7.7) to implicitly step a portion of R^+ forward in the x-direction to the grid point $(x_1, 0)$.

3) To estimate $A(x_1)$ and $B(x_1)$, set $x = x_1$ in (7.9) and (7.10). $W_s(x, 2(1-x)^-)$ is computed by numerical differentiation. In this case, one of these coefficients is found by solving a quadratic equation, and the other is found by simple substitution.

4) Use (7.7) to implicitly step the remaining $R^+(x_0, s)$ data forward in the x-direction to the set of grid points at x_1 for $0 < s < 2(1 - x_1)$.

5) Repeat steps 1-4 to move one grid line deeper into the medium.

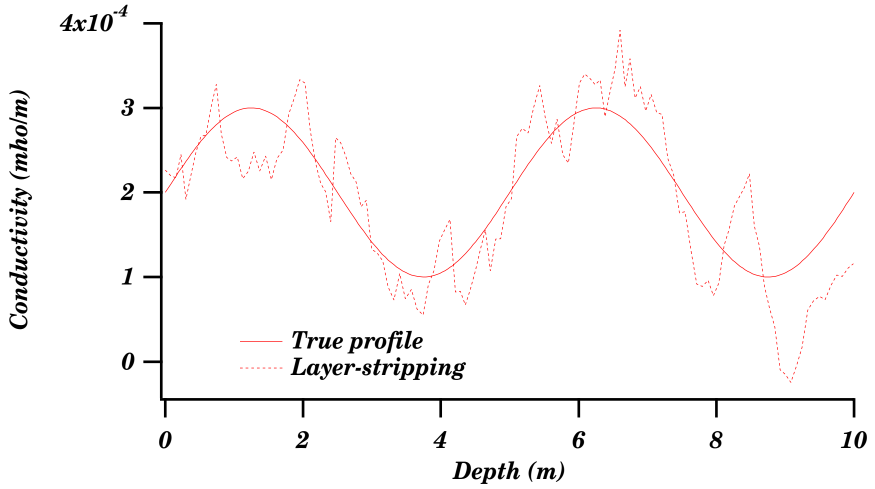

Figure 8: The reconstruction of the conductivity profile without a back wall using noisy data. Gaussian noise with STD=0.05 has been added to the reflection data, R^+, R^-, and the transmission data T. The data are smoothed once before inversion. Three iterations to improve the reconstruction in $A(x)$ and $B(x)$ are made.

The accuracy of this algorithm can be considerably improved through the use of iteration. All that needs to be done is to add the following steps after step 4:

4a) Use (7.8) to implicitly step W from the current grid line x_0 to the next grid line x_1 for $0 < s < 2(1 - x_1)$. This can be done since A, B and R^+ are known (to some degree of accuracy) on the grid lines x_0 and x_1.

4b) Go to step 2.

7.2.2 Downward continuation

The inversion algorithm using the Green functions equations is developed in a similar way to the one in Section 7.2.1 above. The algorithm utilizes the jump discontinuity in the time derivative in the Green function G_1 at $s = 2 - x$.

The Green function G_1 is continuous along the line $s = 2-x$, see (4.4). Therefore,

$$[\partial_x G_1(x,s)]_{s=(2-x)^-}^{s=(2-x)^+} = [\partial_s G_1(x,s)]_{s=(2-x)^-}^{s=(2-x)^+},$$

or using (4.2) and (4.5)

$$[\partial_s G_1(x,s)]_{s=(2-x)^-}^{s=(2-x)^+} = \frac{1}{2} a(1) b^+(x) \exp\left\{ - \int_0^x B(x') d\,x' \right\}, \tag{7.11}$$

where $a(1) = \frac{1}{2} b^-(1) \exp\left\{ \int_0^1 B(x')\, dx' \right\}$. The value of $\partial_s G_1(x,(2-x)^+)$ can be computed using the concept of extension of data in Section 5. Differentiate (5.3) with respect to s and let $s = (2-x)^+$. The result is

$$\begin{aligned}\partial_s G_1(x,(2-x)^+) = W(0,0)\Big\{&W(0,2(1-x)^+)\\ &+\int_x^{2-x} G_1(x,s)W(0,2-x-s)\,ds\Big\}\\ &-W_s(0,2(1-x)^+)-\int_x^{2-x} G_1(x,s)\partial_s W(0,2-x-s)\,ds.\end{aligned}\tag{7.12}$$

The inverse problem using the Green functions equations is solved by the use of the following equations:

$$\begin{cases}\partial_x G_1(x,s)+\partial_s G_1(x,s) = b^+(x)\exp\left\{-\int_0^x B(x')dx'\right\}G_2(x,s),\\ \partial_x G_2(x,s)-\partial_s G_2(x,s) = b^-(x)\exp\left\{\int_0^x B(x')dx'\right\}G_1(x,s),\end{cases}\tag{7.13}$$

for $x < s < 2-x$ and

$$G_2(x,x^+) = -\frac{1}{2}b^-(x)\exp\left\{\int_0^x B(x')dx'\right\},\tag{7.14}$$

$$\begin{aligned}W(0,0)&\left\{W(0,2(1-x)^+)+\int_x^{2-x} G_1(x,s')W(0,2-x-s')\,ds'\right\}\\ &-W_s(0,2(1-x)^+)-\int_x^{2-x} G_1(x,s')\partial_s W(0,2-x-s')\,ds'\\ &-\partial_s G_1(x,(2-x)^-) = \frac{1}{2}a(1)b^+(x)\exp\left\{-\int_0^x B(x')dx'\right\},\end{aligned}\tag{7.15}$$

and where $0 < x < 1$. These four equations are (4.2), (4.3) and a combination of (7.11) and (7.12). $\partial_s G_1(x,(2-x)^-)$ and $W_s(0,s)$ are computed by numerical differentiation and the constant $a(1)$ can be obtained by extension of data in the same way as in Section 7.2.1.

The inversion algorithm using Green functions then proceeds as follows:

1) Use (7.13) to explicitly step G_1 and G_2 from the current grid line x_0 to the next grid line $x_1 = x_0 + h$ for $x_1 < s < 2 - x_1$.

2) To estimate $A(x_1)$ and $B(x_1)$, set $x = x_1$ and use (7.14) and (7.15). The values $\partial_s G_1(x,(2-x)^-)$ and $W_s(0,2(1-x)^+)$ are computed by numerical differentiation. In this case, one of these coefficients is found by solving a quadratic equation, and the other is found by simple substitution.

3) Repeat steps 1 and 2 to move one grid line deeper into the medium.

The accuracy of this algorithm can be considerably improved through the use of iteration. All that needs to be done is to add the following steps after step 2:

2a) Use (7.13) to implicitly step G_1 and G_2 from the current grid line x_0 to the next grid line x_1 for $x_1 < s < 2 - x_1$. This can be done since A and B are known (to some degree of accuracy) on those grid lines.

2b) Go to step 2.

To initiate the inversion algorithm, it is easy to use the following equations to find the unknown $A(0)$ and $B(0)$, see (3.3) and (7.6) for $x = 0$:

$$\begin{aligned} R^+(0) &= -\frac{1}{2}b^-(0), \\ W_s(0, 2^-) &= -\frac{1}{2}b^+(0)a(1). \end{aligned}$$

7.2.3 Numerical experiments

The downward continuation algorithm given in Section 7.2.2 is, in general, one order of magnitude faster compared to the layer-stripping algorithm in Section 7.2.1, due to the absence of convolution integrals in the main equation (7.13).

Figures 9 and 10 illustrate the inversion of noise-free data. It is clearly seen that the algorithm presented in Section 7.1.1 using the complete data set $R^\pm(s)$ and $T(s)$, see Figures 5 and 6, is superior to the algorithms using only one-sided reflection and transmission data, viz. $R^+(s)$ and $T(s)$. No illustrations with noisy data are presented. These algorithms are too sensitive to give any reasonable results with noisy data.

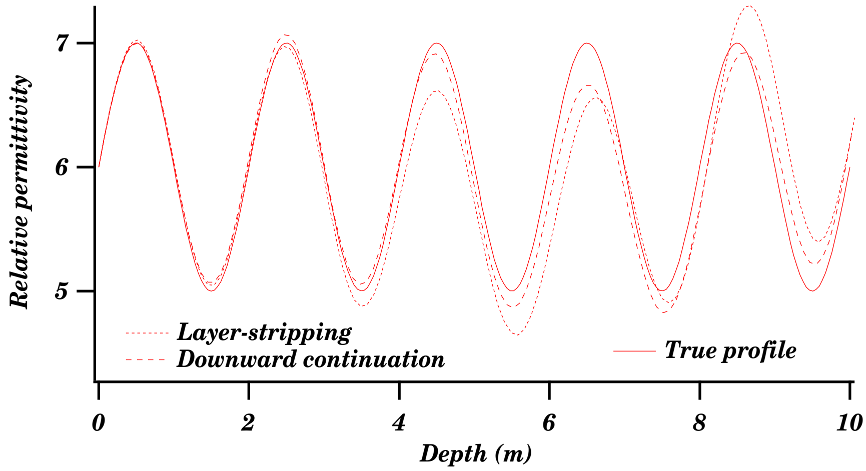

Figure 9: The reconstruction of the relative permittivity profile without a back wall using noise-free R^+ and T data. Three iterations to improve the reconstruction in $A(x)$ and $B(x)$ are made.

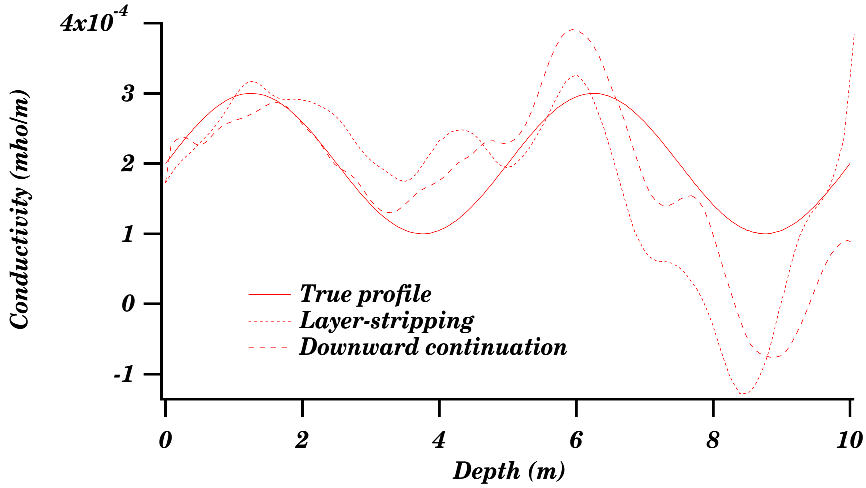

Figure 10: The reconstruction of the conductivity profile without a back wall using noise-free R^+ and T data. Three iterations to improve the reconstruction in $A(x)$ and $B(x)$ are made.

8 Layer-stripping vs. downward continuation in a lossy case with a back wall

A finite jump discontinuity in the permittivity profile at the back edge, $x = 1$, simplifies the inversion algorithms and less data are required to get stable inversion algorithms. The theoretical aspects of this problem using the invariant imbedding equations are developed in Refs. [5, 6]. The main algorithms are summarized and illustrated below. They both rely on the information extracted from the propagator kernel W. Two different ways of obtaining this kernel are given here. The first one, when transmission data are available, is obvious. The resolvent equation (3.6) is solved for W at $x = 0$. The second way of obtaining W is more involved and a Fredholm integral equation of the second kind has to be solved. This method is also, as expected, less stable than the first one that relies on a Volterra integral equation of the second kind.

8.1 T and R^+ data given

The data set for inversion is given in Table 4. This data set consists of two kernels, one reflection and one transmission kernel measured for one round trip, and three constants.

Data set for inversion
$R^+(s), \quad 0 < s < 2$
$T(s), \quad 0 < s < 2$
$\rho(0)$
l
$\epsilon(0)$

Table 4: The first data set for inversion of the discontinuous lossy permittivity profile.

The transmission kernel in this data set is used to obtain the propagator kernel $W(s)$ using the resolvent equation (3.6) at $x = 0$. The constants l and $\epsilon(0)$ are needed to transform the two functions $A(x)$ and $B(x)$ back to the physical quantities $z(x)$, $\epsilon(z)$ and $\sigma(z)$, see (2.3). The constant $\rho(0)$ is assumed to be extracted from the scattering experiments, see (3.1).

8.1.1 Layer-stripping

The algorithm based on the invariant imbedding equations is presented in detail in Refs. [5, 6]. The inverse problem is solved by using the following equations:

$$\begin{aligned}
&R^+_x(x,s) = 2R^+_s(x,s) - B(x)R^+(x,s) \\
&\qquad -b^+(x)\int_0^s R^+(x,s-s')R^+(x,s')d\,x', \quad 0 < s < 2(1-x), && (8.1) \\
&W_x(x,s) = \\
&\qquad b^+(x)\left\{R^+(x,s) + \int_0^s W(x,s-s')R^+(x,s')d\,s'\right\}, \quad 0 < s < 2(1-x), && (8.2) \\
&R^+(x,0^+) = -\frac{1}{2}b^-(x), && (8.3) \\
&W(x,2(1-x)^-) = -\frac{1}{2}\rho(0)b^+(x)\exp\left\{-\int_0^x B(x')\,dx'\right\}, && (8.4)
\end{aligned}$$

and where $0 < x < 1$. These equations are (3.2), (3.7), (3.3) and (3.8).

The inversion algorithm using the invariant imbedding equations then proceeds as follows:

1) Use (8.2) to explicitly step W from the current grid line x_0 to the next grid line $x_1 = x_0 + h$ for $0 < s < 2(1 - x_1)$.

2) Use (8.1) to implicitly step a portion of R^+ forward in the x-direction to the grid point $(x_1, 0)$.

3) To estimate $A(x_1)$ and $B(x_1)$, set $x = x_1$ in (8.3) and (8.4). In this case, one of these coefficients is found by solving a quadratic equation, and the other is found by simple substitution.

4) Use (8.1) to implicitly step the remaining $R^+(x_0, s)$ data forward in the x-direction to the set of grid points at x_1 for $0 < s < 2(1 - x_1)$.

5) Repeat steps 1-4 to move one grid line deeper into the medium.

The accuracy of this algorithm can be considerably improved through the use of iteration. All that needs to be done is to add the following steps after step 4:

4a) Use (8.2) to implicitly step W from the current grid line x_0 to the next grid line x_1 for $0 < s < 2(1-x_1)$. This can be done since A, B and R^+ are known (to some degree of accuracy) on the grid lines x_0 and x_1.

4b) Go to step 2.

8.1.2 Downward continuation

The inversion problem using the Green functions equations is solved by the use of the following equations:

$$\begin{cases} \partial_x G_1(x,s) + \partial_s G_1(x,s) = b^+(x) \exp\left\{-\int_0^x B(x')d\,x'\right\} G_2(x,s), \\ \partial_x G_2(x,s) - \partial_s G_2(x,s) = b^-(x) \exp\left\{\int_0^x B(x')d\,x'\right\} G_1(x,s), \end{cases} \tag{8.5}$$

for $x < s < 2-x$ and

$$G_2(x,x^+) = -\frac{1}{2} b^-(x) \exp\left\{\int_0^x B(x')d\,x'\right\}, \tag{8.6}$$

$$\begin{aligned} &W(0,2(1-x)^+) + \int_x^{2-x} G_1(x,s')W(0,2-x-s')\,ds' + G_1(x,(2-x)^-) \\ &\quad = -\frac{1}{2}\rho(0)b^+(x)\exp\left\{-\int_0^x B(x')\,dx'\right\}, \end{aligned} \tag{8.7}$$

and where $0 < x < 1$. These equations are (4.2), (4.3) and a combination of (5.3), evaluated at $s = (2-x)^+$, and (4.4).

The inversion algorithm using the Green functions then proceeds as follows:

1) Use (8.5) to explicitly step G_1 and G_2 from the current grid line x_0 to the next grid line $x_1 = x_0 + h$ for $x_1 < s < 2 - x_1$.

2) To estimate $A(x_1)$ and $B(x_1)$, set $x = x_1$ and use (8.6) and (8.7). In this case, one of these coefficients is found by solving a quadratic equation, and the other is found by simple substitution.

3) Repeat steps 1 and 2 to move one grid line deeper into the medium.

The accuracy of this algorithm can be considerably improved through the use of iteration. All that needs to be done is to add the following steps after step 2:

2a) Use (8.5) to implicitly step G_1 and G_2 from the current grid line x_0 to the next grid line x_1 for $x_1 < s < 2 - x_1$. This can be done since A and B are known (to some degree of accuracy) on those grid lines.

2b) Go to step 2.

8.1.3 Numerical experiments

The downward continuation algorithm presented in Section 8.1.2 is, in general, one order of magnitude faster that the the layer-stripping algorithm in Section 8.1.1, due to the absence of convolution integrals in the main equation (8.5).

The algorithms based upon the invariant imbedding equations in Section 8.1.1 and the Green functions approach in Section 8.1.2 are illustrated in this section. Figures 11 and 12 give the typical performance of the algorithms using noise-free data. Excellent reconstructions are obtained using the data set in Table 4.

In Figures 13 and 14 the performance of the algorithms in Sections 8.1.1 and 8.1.2 are illustrated using noisy data. Note that the two algorithms both give reconstructions that are very similar (in Figures 13 and 14 the difference are not resolved). The two algorithms, layer-stripping and the downward continuation, are, however, very different. Nevertheless, they both reconstruct almost identical profiles from the noisy reflection and transmission data. This property provides an indication of the stability of the two algorithms.

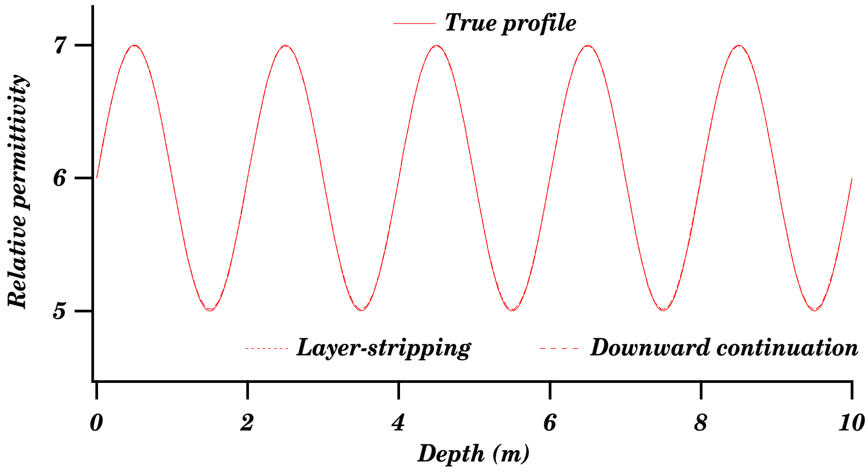

Figure 11: The reconstruction of the relative permittivity profile using noise-free data R^+ and T. The constant $c_1 = 2$. Three iterations to improve the reconstruction in $A(x)$ and $B(x)$ are made.

8.2 R^+ data given for two round trips

In Section 8.1 reflection data and transmission data are used to reconstruct the permittivity and the conductivity profiles. The transmission data are only used to obtain the propagator kernel $W(s)$. It is, however, interesting to find that there is a second independent way of obtaining the propagator kernel $W(s)$ without any transmission data. This data set consists of only reflection data measured for two round trips, see Table 5.

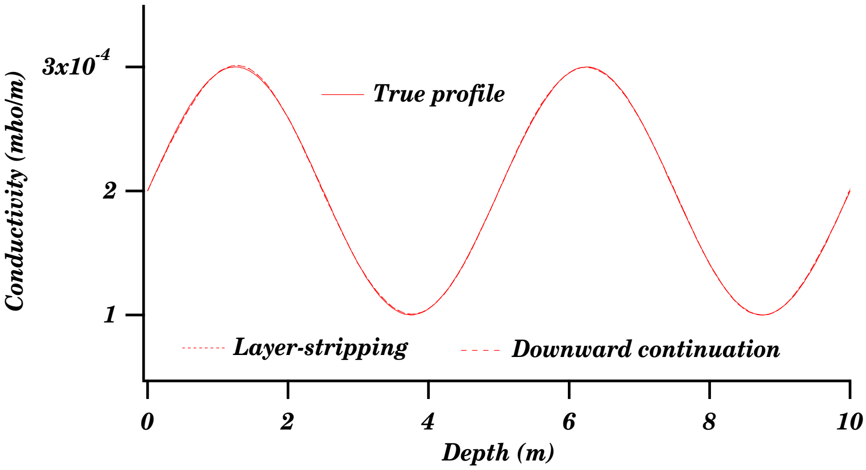

Figure 12: The reconstruction of the conductivity profile using noise-free data R^+ and T. The constant $c_1 = 2$. Three iterations to improve the reconstruction in $A(x)$ and $B(x)$ are made.

Data set for inversion
$R^+(s), \quad 0 < s < 4$
$\rho(0)$
l
$\epsilon(0)$

Table 5: The second data set for inversion of the discontinuous lossy permittivity profile.

Since only reflection data are needed, the receiver and the transmitter are situated on the same side of the slab. In many situations this can be advantageous, e.g. when there is no possibility to access the other side of the slab.

The propagator kernel $W(0, s)$ is then found by solving the following Fredholm integral equation of the second kind:

$$\begin{aligned} &R^+(0, s+2) + \rho(0)W(0, s) \\ &\qquad + \int_0^2 W(0, s')R^+(0, s+2-s')d\,s' = 0, \quad 0 < s < 2. \end{aligned} \tag{8.8}$$

This equation is derived in Ref. [6]. If the reflection kernel $R^+(s)$ is known for two round trips, $0 < s < 4$, then (8.8) is a Fredholm integral equation of the second kind for the unknown propagator kernel $W(s)$, $0 < s < 2$.

The inversion algorithms then proceed exactly as in Sections 8.1.1 and 8.1.2.

8.2.1 Numerical experiments

Figures 15 and 16 illustrate the inversion using noise-free data given by Table 5. Once again, excellent reconstructions are obtained.

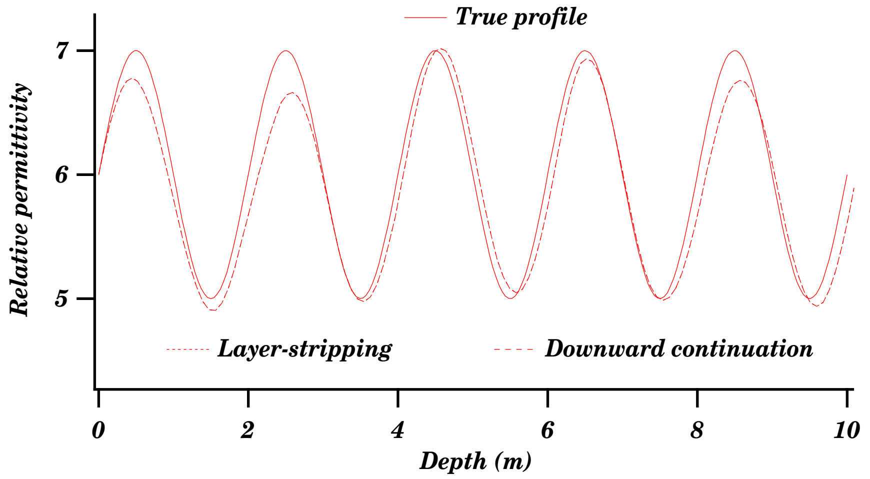

Figure 13: The reconstruction of the relative permittivity profile using noisy data. Gaussian noise with STD=0.05 has been added to the reflection data R^+ and the transmission data T. The data are smoothed once before inversion. The constant $c_1 = 2$. Three iterations to improve the reconstruction in $A(x)$ and $B(x)$ are made.

In Figures 17 and 18 reconstructions using noisy data are depicted. The two algorithms, layer-stripping and downward continuation, both give reconstructions that are very similar (the differences are not resolved in the scale given in the figures). For additional comments, see Section 8.1.3. A comparison between the reconstructions in this section using data in Table 5, and the reconstructions in Section 8.1 using data given in Table 4, immediately shows that the latter data set gives more accurate reconstructions. This becomes obvious when noisy data are used, compare Figures 13 and 14 and Figures 17 and 18. This difference in accuracy is due to the way the propagator kernel is obtained. In Section 8.1 the propagator kernel was obtained by solving a Volterra integral equation of the second kind, see (3.6), but in this section a Fredholm integral equation of the second kind, see (8.8), is solved.

9 Conclusions

In this paper a review of transient electromagnetic wave propagation in lossy slabs is presented. Some old algorithms are discussed and several new ones are presented. In particular, the numerical performances of the algorithms have been compared for both noise-free and noisy data. In an Appendix some new results on integral identities and inequalities using time reversal arguments are presented.

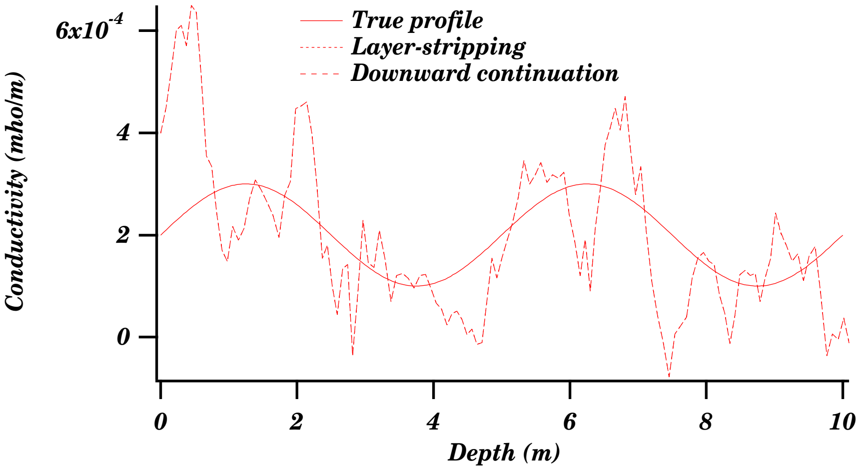

Figure 14: The reconstruction of the conductivity profile using noisy data. Gaussian noise with STD=0.05 has been added to the reflection data R^+ and the transmission data T. The data are smoothed once before inversion. The constant $c_1 = 2$. Three iterations to improve the reconstruction in $A(x)$ and $B(x)$ are made.

Appendix A Time reversal results for the lossless slab

In this appendix some new results are presented using time reversion arguments. The slab is in this entire appendix assumed to be lossless and continuous, i.e., $B(x) = 0$ and $c_1 = 1$. Consider a two way excitation of the slab; one from the left, $u^+(0,s)$, and one from the right, $u^-(1,s)$, see the space-time diagram in Figure 20.

The relation between the excitation and the response is represented as the scattering operators [2][2]

$$\begin{aligned} u^-(0,s) &= \int_{-\infty}^{s} R^+(s-s')u^+(0,s')d\,s' \\ &\quad + t^+\left\{u^-(1,s-1) + \int_{-\infty}^{s-1} T(s-1-s')u^-(1,s')d\,s'\right\}, \qquad \text{(A.1)} \\ u^+(1,s) &= \int_{-\infty}^{s} R^-(s-s')u^-(1,s')d\,s' \\ &\quad + t^-\left\{u^+(0,s-1) + \int_{-\infty}^{s-1} T(s-1-s')u^+(0,s')d\,s'\right\}, \qquad \text{(A.2)} \end{aligned}$$

where

$$t^{\pm} = \exp\left\{\pm\frac{1}{2}\int_0^1 A(x')d\,x'\right\}.$$

---

[2] In Ref. [3] it is shown that the two transmission kernels (transmission from left to right and from right to left, respectively) are identical.

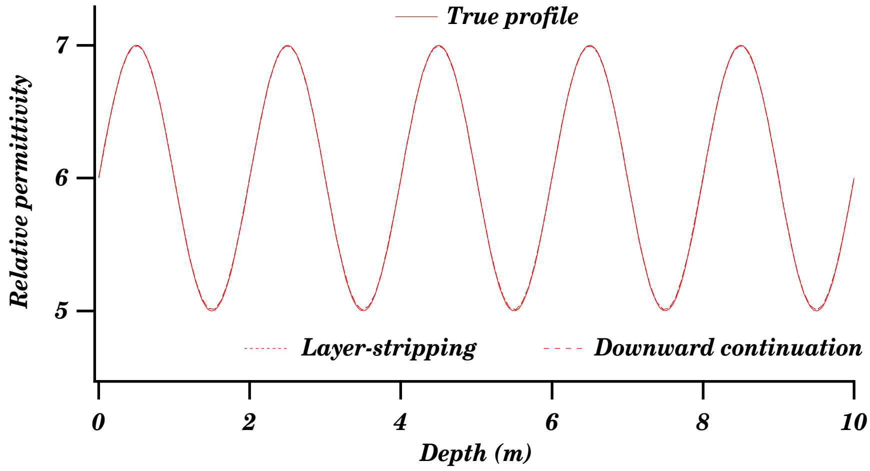

Figure 15: The reconstruction of the relative permittivity profile using noise-free reflection data R^+ for two round trips. The constant $c_1 = 2$. Three iterations to improve the reconstruction in $A(x)$ and $B(x)$ are made.

In the time reversed configuration of the original problem the excitations, $u^+(0,s)$ and $u^-(1,s)$, and the responses, $u^-(0,s)$ and $u^+(1,s)$, are reversed, see Figure 19. The following representations hold since the underlying PDE, see (2.2) with $B(x) = 0$, is invariant under time reversion and the scattering kernels $R^+(s)$, $T(s)$ and $R^-(s)$ are independent of the excitation:

$$\begin{aligned} u^+(0,-s) &= \int_{-\infty}^{s} R^+(s-s')u^-(0,-s')d\,s' \\ &\quad + t^+\left\{u^+(1,-(s-1)) + \int_{-\infty}^{s-1} T(s-1-s')u^+(1,-s')d\,s'\right\}, \qquad \text{(A.3)} \\ u^-(1,-s) &= \int_{-\infty}^{s} R^-(s-s')u^+(1,-s')d\,s' \\ &\quad + t^-\left\{u^-(0,-(s-1)) + \int_{-\infty}^{s-1} T(s-1-s')u^-(0,-s')d\,s'\right\}. \qquad \text{(A.4)} \end{aligned}$$

Insert (A.1) and (A.2) into (A.3) and (A.4). Since the excitations, $u^+(0,s)$ and $u^-(1,s)$, are arbitrary the following identities for the reflection kernels $R^\pm(s)$ and

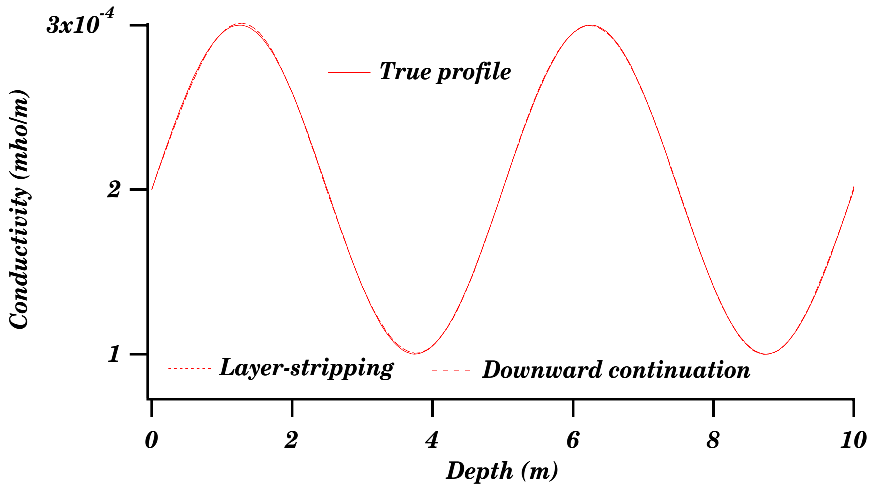

Figure 16: The reconstruction of the conductivity profile using noise-free reflection data R^+ for two round trips. The constant $c_1 = 2$. Three iterations to improve the reconstruction in $A(x)$ and $B(x)$ are made.

the transmission kernel $T(s)$ are derived:

$$\begin{aligned} &H(s)T(s) + H(-s)T(-s) + \int_{\max(0,-s)}^{\infty} T(s')T(s+s')\,ds' \\ &\quad + \int_{\max(0,-s)}^{\infty} R^{\pm}(s')R^{\pm}(s+s')\,ds' = 0, \\ &H(s)R^{\pm}(s) + H(2-s)R^{\mp}(2-s) + \int_{\max(0,-s)}^{\infty} T(s')R^{\pm}(s+s')\,ds' \\ &\quad + \int_{\max(0,s-2)}^{\infty} T(s')R^{\mp}(2-s+s')\,ds' = 0, \end{aligned} \tag{A.5}$$

where $H(s)$ is the Heaviside function. In the first equation there is no loss of generality to assume that $s > 0$ and the first equation then simplifies to

$$T(s) + \int_0^{\infty} T(s')T(s+s')\,ds' + \int_0^{\infty} R^{\pm}(s')R^{\pm}(s+s')\,ds' = 0, \quad s > 0. \tag{A.6}$$

From (3.5) and (3.3) it is easy to calculate the value of the transmission kernel at $s = 0^+$. Then take the $s \longrightarrow 0^+$ limit in (A.6). The result is

$$\int_0^{\infty} \left\{ |T(s')|^2 + |R^{\pm}(s')|^2 \right\} ds' = \frac{1}{8} \int_0^1 A^2(x)\,dx,$$

from which it is seen that the reflection kernels $R^{\pm}(s)$ and the transmission kernel $T(s)$ are all square-integrable functions of the variable s. Additionally,

$$\int_0^{\infty} |R^+(s')|^2\,ds' = \int_0^{\infty} |R^-(s')|^2\,ds'.$$

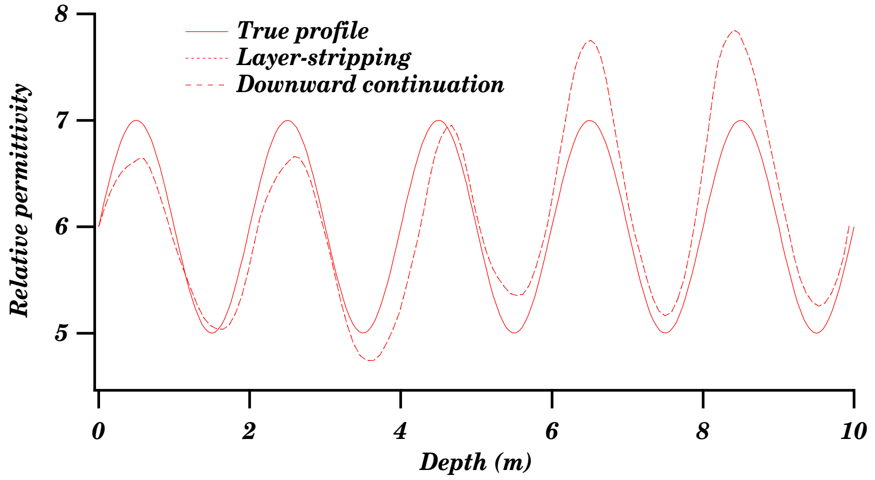

Figure 17: The reconstruction of the relative permittivity profile using noisy reflection data R^+ for two round trips. Gaussian noise with STD=0.05 has been added to the reflection data R^+. The data are smoothed once before inversion. The constant $c_1 = 2$. Three iterations to improve the reconstruction in $A(x)$ and $B(x)$ are made.

Moreover, equation (A.6) immediately implies that

$$\int_0^\infty R^+(s')R^+(s+s')\,ds' = \int_0^\infty R^-(s')R^-(s+s')\,ds', \quad s>0.$$

Furthermore, an application of the Hölder's inequality gives

$$\left|\int_0^\infty T(s')T(s+s')\,ds'\right|^2 \le \int_0^\infty |T(s')|^2\,ds' \int_s^\infty |T(s')|^2\,ds',$$

and similarly for the kernels $R^\pm(s)$. From this inequality and (A.6) it is possible to estimate the absolute value of the transmission kernel for all $s>0$.

$$\begin{aligned}|T(s)| &\le \left|\int_0^\infty T(s')T(s+s')\,ds'\right| + \left|\int_0^\infty R^\pm(s')R^\pm(s+s')\,ds'\right| \\ &\le \sqrt{\int_0^\infty |T(s')|^2\,ds' \int_s^\infty |T(s')|^2\,ds'} + \sqrt{\int_0^\infty |R^\pm(s')|^2\,ds' \int_s^\infty |R^\pm(s')|^2\,ds'}.\end{aligned}$$

This inequality shows that

$$T(s)\to 0, \quad s\to\infty,$$

and

$$|T(s)| \le \int_0^\infty \left\{|T(s')|^2 + |R^\pm(s')|^2\right\}\,ds' = \frac{1}{8}\int_0^1 A^2(x)\,dx.$$

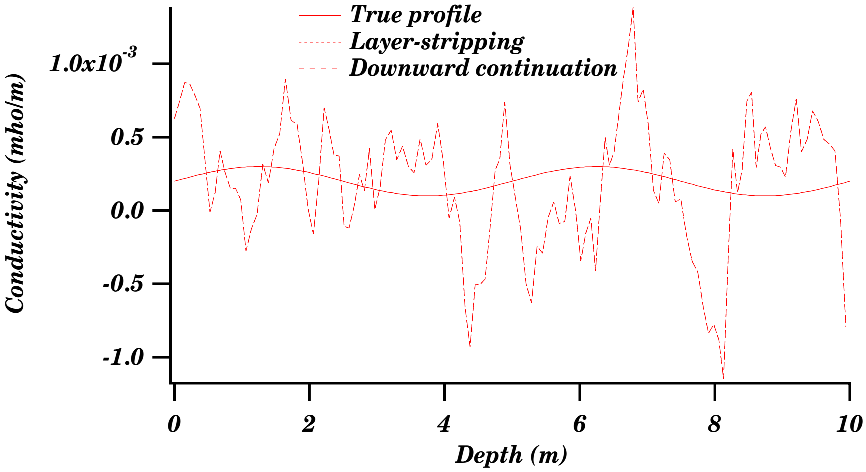

Figure 18: The reconstruction of the conductivity profile using noisy reflection data R^+ for two round trips. Gaussian noise with STD=0.05 has been added to the reflection data R^+. The data are smoothed once before inversion. The constant $c_1 = 2$. Three iterations to improve the reconstruction in $A(x)$ and $B(x)$ are made.

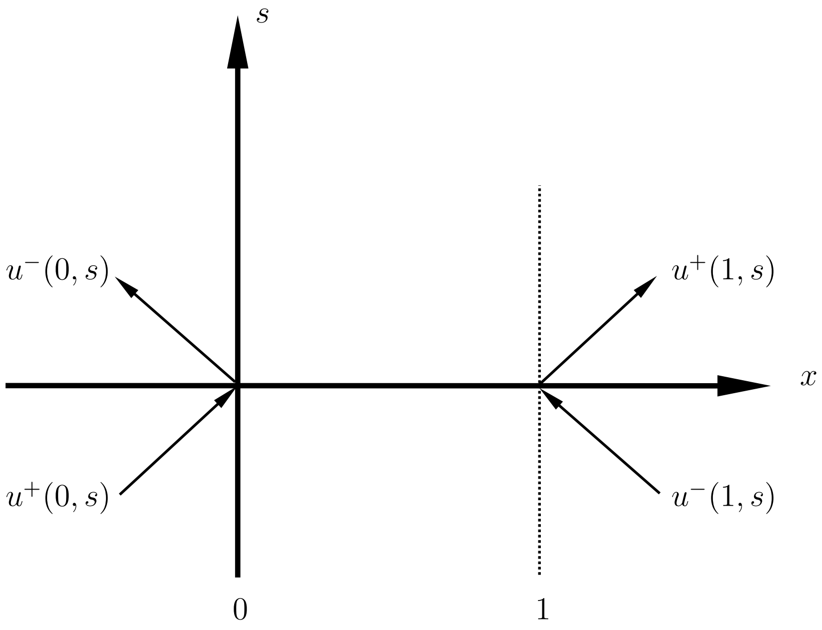

Figure 19: Space-time diagram for the original problem.

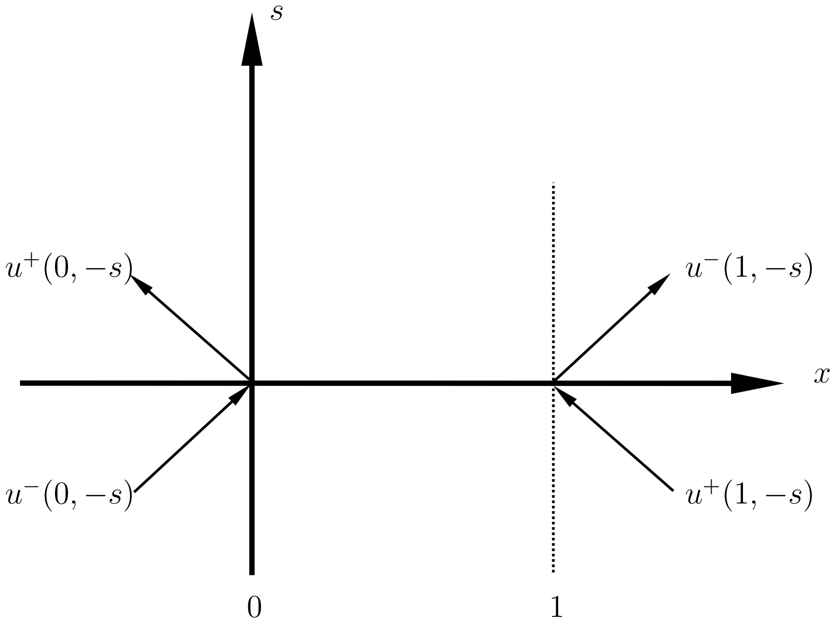

Figure 20: Space-time diagram for the time-reversed problem.

In an analogous way, it is straightforward to prove the following results from (A.5) for the reflection kernels $R^\pm(s)$ for $s > 2$:

$$|R^\pm(s)| \le \sqrt{\int_0^\infty |T(s')|^2\,ds' \int_s^\infty |R^\pm(s')|^2\,ds'} + \sqrt{\int_0^\infty |R^\mp(s')|^2\,ds' \int_{s-2}^\infty |T(s')|^2\,ds'}.$$

This implies that

$$R^\pm(s) \to 0, \quad s \to \infty,$$

and

$$|R^\pm(s)| \le 2\sqrt{\int_0^\infty |T(s')|^2\,ds' \int_0^\infty |R^\pm(s')|^2\,ds'} \le \frac{1}{8}\int_0^1 A^2(x)\,dx, \quad s > 2,$$

since

$$\begin{aligned}&\frac{1}{8}\int_0^1 A^2(x)\,dx - 2\sqrt{\int_0^\infty |T(s')|^2\,ds'}\sqrt{\int_0^\infty |R^\pm(s')|^2\,ds'}\\ &\quad = \left\{\sqrt{\int_0^\infty |T(s')|^2\,ds'} - \sqrt{\int_0^\infty |R^\pm(s')|^2\,ds'}\right\}^2 \ge 0.\end{aligned}$$

References

[1] J.P. Corones, M.E. Davison, and R.J. Krueger. Wave splittings, invariant imbedding and inverse scattering. In A.J. Devaney, editor, *Inverse Optics*, pages 102–106, SPIE Bellingham, WA, 1983. Proc. SPIE 413.

[2] J.P. Corones and R.J. Krueger. Obtaining scattering kernels using invariant imbedding. *J. Math. Anal. Appl.*, 95:393–415, 1983.

[3] G. Kristensson and R.J. Krueger. Direct and inverse scattering in the time domain for a dissipative wave equation. part 1: Scattering operators. *J. Math. Phys.*, 27(6):1667–1682, 1986.

[4] G. Kristensson and R.J. Krueger. Direct and inverse scattering in the time domain for a dissipative wave equation. part 2: Simultaneous reconstruction of dissipation and phase velocity profiles. *J. Math. Phys.*, 27(6):1683–1693, 1986.

[5] G. Kristensson and R.J. Krueger. Direct and inverse scattering in the time domain for a dissipative wave equation. part 3: Scattering operators in the presence of a phase velocity mismatch. *J. Math. Phys.*, 28(2):360–370, 1987.

[6] G. Kristensson and R.J. Krueger. Direct and inverse scattering in the time domain for a dissipative wave equation. part 4: Use of phase velocity mismatches to simplify inversions. *Inverse Problems*, 5(3):375–388, 1989.

[7] R.J. Krueger and R.L. Ochs, Jr. A Green's function approach to the determination of internal fields. *Wave Motion*, 11:525–543, 1989.